












## Magnetic Fields in the Infrared Dark Cloud G34.43+0.24

Archana Soam<sup>1,2</sup> , Tie Liu<sup>3</sup> , B-G Andersson<sup>1</sup> , Chang Won Lee<sup>2,4</sup> , Junhao Liu<sup>5,6,7</sup> , Mika Juvela<sup>8</sup> , Pak Shing Li<sup>9</sup> , Paul F. Goldsmith<sup>10</sup> , Qizhou Zhang<sup>7</sup> , Patrick M. Koch<sup>11</sup> , Kee-Tae Kim<sup>2,4</sup> , Keping Qiu<sup>5,6</sup> , Neal J. Evans II<sup>2,12,13</sup> , Doug Johnstone<sup>14,15</sup> , Mark Thompson<sup>16</sup> , Derek Ward-Thompson<sup>17</sup> , James Di Francesco<sup>14,15</sup> , Ya-Wen Tang<sup>11</sup> , Julien Montillaud<sup>18</sup> , Gwanjeong Kim<sup>19</sup> , Steve Mairs<sup>20</sup> , Patricio Sanhueza<sup>21</sup> , Shinyoung Kim<sup>2,4</sup> , David Berry<sup>20</sup> , Michael S. Gordon<sup>1</sup> , Ken'ichi Tatematsu<sup>21</sup> , Sheng-Yuan Liu<sup>11</sup> , Kate Pattle<sup>22</sup> , David Eden<sup>23</sup> , Peregrine M. McGehee<sup>24</sup> , Ke Wang<sup>25</sup> , I. Ristorcelli<sup>26</sup> , Sarah F. Graves<sup>20</sup> , Dana Alina<sup>27</sup> , Kevin M. Lacaille<sup>28,29</sup> , Ludovic Montier<sup>26</sup> , Geumsook Park<sup>2</sup> , Woojin Kwon<sup>2,4</sup> , Eun Jung Chung<sup>2</sup> , Veli-Matti Pelkonen<sup>8,30</sup> , Elisabetta R. Micelotta<sup>8</sup> , Mika Saajasto<sup>8</sup> , and Gary Fuller<sup>31</sup> 

<sup>1</sup> SOFIA Science Centre, USRA, NASA Ames Research Centre, MS-12, N232, Moffett Field, CA 94035, USA; [asoam@usra.edu](mailto:asoam@usra.edu), [archanasoam.bhu@gmail.com](mailto:archanasoam.bhu@gmail.com)

<sup>2</sup> Korea Astronomy and Space Science Institute, 776 Daedeokdae-ro, Yuseong-gu, Daejeon 34055, Republic of Korea

<sup>3</sup> Shanghai Astronomical Observatory, Chinese Academy of Sciences, 80 Nandan Road, Shanghai 200030, People's Republic of China

<sup>4</sup> University of Science and Technology, Korea (UST), 217 Gajeong-ro, Yuseong-gu, Daejeon 34113, Republic of Korea

<sup>5</sup> School of Astronomy and Space Science, Nanjing University, 163 Xianlin Avenue, Nanjing 210023, People's Republic Of China

<sup>6</sup> Key Laboratory of Modern Astronomy and Astrophysics (Nanjing University), Ministry of Education, Nanjing 210023, People's Republic Of China

<sup>7</sup> Harvard-Smithsonian Center for Astrophysics, 60 Garden Street, Cambridge, MA 02138, USA

<sup>8</sup> Department of Physics, P.O. Box 64, FI-00014, University of Helsinki, Finland

<sup>9</sup> University of California, Berkeley, USA

<sup>10</sup> Jet Propulsion Laboratory, California Institute of Technology, Pasadena, CA 90039, USA

<sup>11</sup> Academia Sinica Institute of Astronomy and Astrophysics, P.O. Box 23-141, Taipei 10617, Taiwan

<sup>12</sup> Department of Astronomy, The University of Texas at Austin, 2515 Speedway, Stop C1400, Austin, TX 78712-1205, USA

<sup>13</sup> Humanitas College, Global Campus, Kyung Hee University, Yongin-shi 17104, Republic of Korea

<sup>14</sup> NRC Herzberg Astronomy and Astrophysics, 5071 West Saanich Road, Victoria, BC V9E 2E7, Canada

<sup>15</sup> Department of Physics and Astronomy, University of Victoria, Victoria, BC V8P 1A1, Canada

<sup>16</sup> University of Hertfordshire (Centre for Astrophysics Research), UK

<sup>17</sup> Jeremiah Horrocks Institute, University of Central Lancashire, Preston PR1 2HE, UK

<sup>18</sup> Institut UTINAM—UMR 6213—CNRS—Univ Bourgogne Franche Comte, OSU THETA, 41bis avenue de l'Observatoire, F-25000 Besançon, France

<sup>19</sup> Nobeyama Radio Observatory, National Astronomical Observatory of Japan, National Institutes of Natural Sciences, Nobeyama, Minamimaki, Minamisaku, Nagano 384-1305, Japan

<sup>20</sup> East Asian Observatory, 660 N. A'ohōkū Place, University Park, Hilo, HI 96720, USA

<sup>21</sup> National Astronomical Observatory of Japan, National Institutes of Natural Sciences, 2-21-1 Osawa, Mitaka, Tokyo 181-8588, Japan

<sup>22</sup> Institute of Astronomy and Department of Physics, National Tsing Hua University, Hsinchu 30013, Taiwan

<sup>23</sup> Astrophysics Research Institute, Liverpool John Moores University, IC2, Liverpool Science Park, 146 Brownlow Hill, Liverpool L3 5RF, UK

<sup>24</sup> Department of Earth and Space Sciences, College of the Canyons, Santa Clarita, CA 91355, USA

<sup>25</sup> Kavli Institute for Astronomy and Astrophysics, Peking University, 5 Yiheyuan Road, Haidian District, Beijing 100871, People's Republic of China

<sup>26</sup> Institut pour la Recherche en Astrophysique et Planétologie, France

<sup>27</sup> Nazarbayev University, Kabanbay batyr ave, 53, Nur-Sultan, 010000, Kazakhstan

<sup>28</sup> Department of Physics and Astronomy, McMaster University, Hamilton, ON L8S 4M1, Canada

<sup>29</sup> Department of Physics and Atmospheric Science, Dalhousie University, Halifax B3H 4R2, Canada

<sup>30</sup> Institut de Ciències del Cosmos, Universitat de Barcelona, IEEC-UB, Martí Franquès 1, E-08028 Barcelona, Spain

<sup>31</sup> Jodrell Bank Centre for Astrophysics, School of Physics and Astronomy, University of Manchester, Oxford Road, Manchester, M13 9PL, UK

<sup>32</sup> East Asian Observatory, 660 N. A'ohoku Place, Hilo, HI 96720, USA

Received 2018 December 31; revised 2019 August 6; accepted 2019 August 7; published 2019 September 24

### Abstract

We present the  $B$ -fields mapped in IRDC G34.43+0.24 using 850  $\mu\text{m}$  polarized dust emission observed with the POL-2 instrument at the James Clerk Maxwell telescope. We examine the magnetic field geometries and strengths in the northern, central, and southern regions of the filament. The overall field geometry is ordered and aligned closely perpendicular to the filament's main axis, particularly in regions containing the central clumps MM1 and MM2, whereas MM3 in the north has field orientations aligned with its major axis. The overall field orientations are uniform at large (POL-2 at 14'' and SHARP at 10'') to small scales (TADPOL at 2''5 and SMA at 1''5) in the MM1 and MM2 regions. SHARP/CSO observations in MM3 at 350  $\mu\text{m}$  from Tang et al. show a similar trend as seen in our POL-2 observations. TADPOL observations demonstrate a well-defined field geometry in MM1/MM2 consistent with MHD simulations of accreting filaments. We obtained a plane-of-sky magnetic field strength of  $470 \pm 190 \mu\text{G}$ ,  $100 \pm 40 \mu\text{G}$ , and  $60 \pm 34 \mu\text{G}$  in the central, northern, and southern regions of G34, respectively, using the updated Davis–Chandrasekhar–Fermi relation. The estimated value of field strength, combined with column density and velocity dispersion values available in the literature, suggests G34 to be marginally critical with criticality parameter  $\lambda$  values  $0.8 \pm 0.4$ ,  $1.1 \pm 0.8$ , and  $0.9 \pm 0.5$  in the central, northern, and southern regions, respectively. The turbulent motions in G34 are sub-Alfvénic with Alfvénic Mach numbers of  $0.34 \pm 0.13$ ,  $0.53 \pm 0.30$ , and  $0.49 \pm 0.26$  in the three regions. The observed aligned  $B$ -fields in G34.43+0.24 are consistent with theoretical models suggesting that  $B$ -fields play an important role in guiding the contraction of the cloud driven by gravity.

**Key words:** ISM: magnetic fields

## 1. Introduction

Filamentary structures exist in molecular clouds, with sizes ranging from a few to tens of parsecs (André et al. 2014; Wang et al. 2016). Recent magnetohydrodynamic (MHD) simulations (Klassen et al. 2017; Gómez et al. 2018; Li et al. 2018) probing the formation of large-scale filamentary clouds suggest a complex evolutionary process involving the interaction and fragmentation of dense, velocity-coherent, fibers into chains of cores, resembling observations in nearby clouds (e.g., L1495/B213 and Musca cloud; Hacar et al. 2013, 2016). The simulations show that global magnetic fields are expected to be roughly perpendicular to the longer axes of dense filamentary clouds. Several velocity-coherent fibers are identified inside the clouds and appear to be supportable along the main filament. In 3D MHD simulations of cluster-forming turbulent molecular cloud clumps, Klassen et al. (2017) found that  $B$ -fields are oriented parallel to subvirial clouds and perpendicular to denser gravitationally bound clouds.

Recent ideal MHD simulations by Li & Klein (2019) found that the magnetic field helps in shaping the long filamentary structures with field orientation perpendicular to the long axis of the filaments. Their simulation produces fiber-like substructures similar to those observed in L1495 (Hacar et al. 2013). There are some other MHD simulations available that include magnetic fields in filaments. Federrath et al. (2016) presented MHD simulations studying the effect of magnetic fields, gravity, and turbulence on the formation of filaments finding that filament width does not depend on the orientation of filament with respect to the magnetic fields in G0.253+0.016 region. A statistical analysis of nearby clouds such as Taurus, Musca, Ophiuchus, and Chameleon has revealed that  $B$ -field lines tend to become parallel to the filament long axes at low densities (or “diffuse” with a few  $\text{cm}^{-3}$ ; e.g., Chapman et al. 2011; Planck Collaboration et al. 2015, 2016; Cox et al. 2016) but are perpendicular to the denser filamentary structures. Koch et al. (2014) presented a statistical analysis of 50 sources (from 4000 independent measurements observed with the SMA and the CSO) on the scales of 0.1–0.01 pc with densities  $\gtrsim 10^5 \text{ cm}^{-3}$ . Their analysis of  $B$ -fields and intensity gradients reveals that the field orientation is perpendicular to the sources’ major axes.

Polarized thermal dust emission at submillimeter wavelengths probes the magnetic field structure in high-density regions. The Radiative Torque Alignment theory of grain alignment is currently one of the most promising models to explain the polarization of light toward clouds and cores (Dolginov & Mitrofanov 1976; Lazarian et al. 1997). This model predicts that the asymmetric nonspherical dust grains rotate due to radiative torque and align with their long axes perpendicular to ambient magnetic field. Due to low angular resolution (e.g.,  $\sim 5'$  with Planck) or high dust extinction (optical or near-infrared polarimetry), previous studies of magnetic fields in filamentary clouds have been mostly limited to nearby clouds. So far, magnetic fields have only been investigated in a few infrared dark clouds (Pillai et al. 2015; Juvela et al. 2018; Liu et al. 2018a, 2018b). Additional observations with higher angular resolution toward filamentary clouds and cores are still needed.

To this end, we are conducting a series of dust polarization observations toward the brightest filaments identified in the James Clerk Maxwell telescope (JCMT) legacy survey of  $\sim 1000$  Planck Galactic Cold Clumps (PGCCs), called SCOPE (SCUBA-2 Continuum Observations of Pre-protostellar

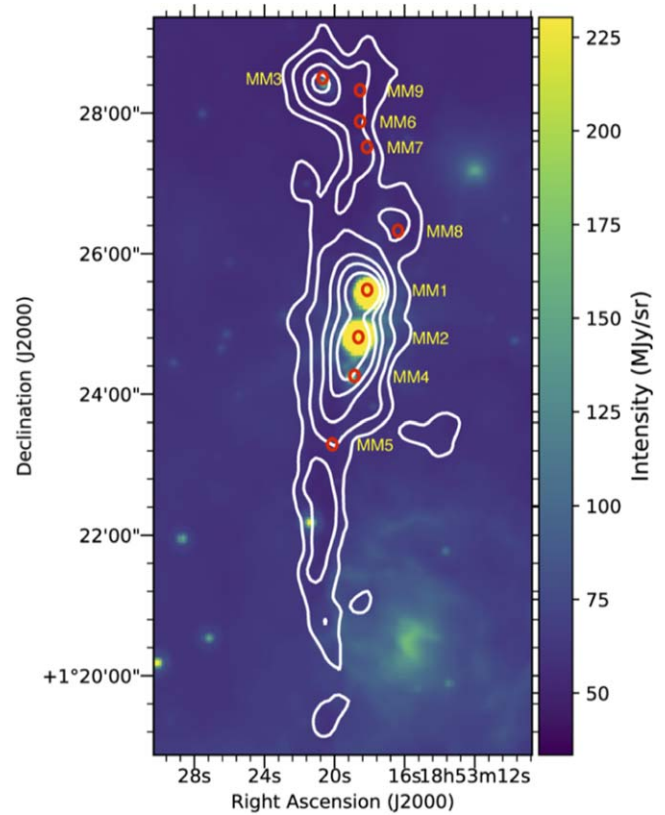


**Figure 1.** *Spitzer* 24  $\mu\text{m}$  image of G34 filament overlaid with JCMT 850  $\mu\text{m}$  contours with levels at 45, 144, 418, 800, and 1500  $\text{mJy beam}^{-1}$ . The millimeter cores identified by Rathborne et al. (2006) are shown as red open circles and are labeled as MM1–MM9.

Evolution; Liu et al. 2018c; Eden et al. 2019), with the POL-2 polarimeter at the JCMT. The observational results of two PGCCs, G35.49–0.31 (hereafter G35) and G9.62+0.19 (hereafter G9) are published in Liu et al. (2018a, 2018b), respectively.

In this work, we report POL-2 observational results toward a more evolved filament, G34.43+0.24 (hereafter G34). At a distance of  $\sim 3.7$  kpc (Sanhueza et al. 2012; Foster et al. 2014; Xu et al. 2016), G34 is an active high-mass star-forming filamentary cloud (Molinari et al. 1998; Rathborne et al. 2011; Sakai et al. 2018). G34 harbors multiple cores, including G34-MM1 through MM9, that are likely at different evolutionary stages (Chen et al. 2011). Figure 1 shows the locations of these MM sources. G34-MM2 was found to be the most evolved core (Rathborne et al. 2006) associated with the ultra-compact H II (UCH II) region IRAS 18507+0121 of spectral type B0.5 (Molinari et al. 1998; Shepherd et al. 2004, 2007). Investigating the cores in G34, Rathborne et al. (2008) found that the brightest millimeter core, G34-MM1, exhibits a typical chemical signature of a high-mass core. On the other hand, the clump MM3 hosts a hot-corino (Yanagida et al. 2014; Sakai et al. 2015). Chambers et al. (2009) found G34-MM1, MM3, MM4, MM5, and MM8 associated with extended *Spitzer* 4.5  $\mu\text{m}$  emissions, indicating possible outflow activities. Sanhueza et al. (2010) also observed these cores and found molecular outflows associated with cores G34-MM1, MM2, MM3, and MM4. G35 is a filament similar to G34 with several embedded low-luminosity massive protostars (Nguyen Luong et al. 2011) and massive starless clumps (Liu et al. 2018a). A

network of filaments covering a broad range of densities is also revealed in G35. The magnetic field lines in G35 tend to be perpendicular to the densest part of the most massive filament, whereas they tend to be parallel in the low-density regions as well as in other less dense filaments (Liu et al. 2018a). The magnetic fields together with turbulence, however, do not appear able to support against the gravitational collapse of the densest clumps in G35. The northern region of G34 with MM3 is associated with the PGCC G34.50 +0.27. G34 has a mass per unit length of  $\sim 1600 M_{\odot} \text{ pc}^{-1}$  (Xu et al. 2016), which is about four times larger than that ( $\sim 410 M_{\odot} \text{ pc}^{-1}$ ) of G35 (Liu et al. 2018a). By comparing G34 with G35, we can determine which of the three mechanisms,  $B$ -fields, gravity, or turbulence, is dominant in filament evolution and dense core formation.

## 2. Observations, Data Acquisition, Reduction, and Validation

The POL-2 observations were conducted in 2018 August (M18AP041; PI: Soam A.) in Band-2 weather conditions using the POL-2 daisy map mode of JCMT (Holland et al. 2013; Friberg et al. 2016; P. Bastien et al. 2019, in preparation) at  $850 \mu\text{m}$ . In this mode of observations, a fully sampled circular region of  $11'$  diameter is produced with a high signal-to-noise coverage over the central  $3'$  of the map. This observing mode is based on the SCUBA-2 CV daisy scan pattern (Holland et al. 2013) but modified to have a slower scan speed (i.e.,  $8''/\text{s}$  compared to  $155''/\text{s}$ ) to obtain sufficient on-sky data for good Stokes  $Q$  and  $U$  values. Coverage decreases, with a consequent significant increase in the rms noise, toward the edges of the map. The POL-2 polarimeter with a rotating half-wave plate at a frequency of 2 Hz and a fixed polarizer is placed in the optical path of the SCUBA-2 camera. The total on-source integration time was  $\sim 3$  hr with  $\tau_{225}$  ranging from 0.05 to 0.08, where  $\tau_{225}$  is atmospheric opacity at 225 GHz. We adopted the same observational strategy as that described by Ward-Thompson et al. (2017). POL-2 simultaneously collects the data at  $450 \mu\text{m}$  and  $850 \mu\text{m}$  wavelengths with full-width half maximum (FWHM) of  $9''.6$  and  $14''.1$ , respectively (Dempsey et al. 2013). We have not reported  $450 \mu\text{m}$  data in this work since the instrumental polarization (IP) model for  $450 \mu\text{m}$  data was not commissioned when this project started.

The data were acquired from the Canadian Astronomy Data Center and reduced using the STARLINK/SMURF package `pol2map` (Chapin et al. 2013; Currie et al. 2014) specifically developed for reducing submillimeter data obtained from JCMT. The details of the data reduction steps and procedure are described in Wang et al. (2019). In the first run of `pol2map`, the raw bolometer time-streams for each observation are converted into separate Stokes  $Q$ ,  $U$ , and  $I$  time-streams using the process `calcqu`. Then a Stokes  $I$  map is created from all  $I$  time-streams using a routine `makemap`, which is an iterative map-making process in the SMURF package. Individual  $I$  maps corresponding to each observation were coadded to produce the initial  $I$  map of the region. The details of this step can be seen in Chapin et al. (2013). The final  $I$ ,  $Q$ , and  $U$  maps were obtained by running `pol2map` a third time. The initial  $I$  map described in a previous step is used to generate a fixed signal-to-noise ratio (S/N)-based mask for all further iterations of `makemap`. The pointing corrections determined in the previous step were applied during the map-making process. During the final process, we invoked an

additional parameter called `skyloop`<sup>33</sup> in `pol2map` and corrected for the loss of synchronization between data values and pointing information in the data reduction process. `Skyloop` improves the recovery of faint, extended structures by performing one iteration of the `mapmaker` on all of the observations, coadding the result, and testing each successive iteration for convergence (see Wang et al. 2019). This is in contrast to the traditional map-making method of deriving an iterative solution for each observation individually. The final polarization values obtained here are debiased by using the mean of  $Q$  and  $U$  variances to remove statistical bias in regions of low S/N.

The calibrated  $I$ ,  $Q$ , and  $U$  maps were obtained in Jy beam<sup>-1</sup> units using a flux calibration factor of  $537 \text{ Jy pW}^{-1}$  given for  $850 \mu\text{m}$ . The output maps are multiplied by 1.35 to account for additional losses due to POL-2 (Dempsey et al. 2013; Friberg et al. 2016). The final coadded total intensity map has an rms noise<sup>34</sup> of  $\sim 7.0 \text{ mJy beam}^{-1}$ . The rms noise in  $Q$  and  $U$  maps were found to be  $\sim 7.9 \text{ mJy beam}^{-1}$  and  $\sim 6.8 \text{ mJy beam}^{-1}$ , respectively.

After the final step of running `pol2map`, we obtain a polarization vector catalog that is produced by coadding Stokes  $I$ ,  $Q$ , and  $U$  maps. The data were reduced with a  $4''$  pixel size but to improve the sensitivity, we binned the coadded Stokes  $I$ ,  $Q$ , and  $U$  maps to  $12''$  pixel size using binning over  $3 \times 3$  pixels.

The debiased (Wardle & Kronberg 1974) polarization fraction values were estimated (see Soam et al. 2018; Wang et al. 2019) as

$$P = \frac{1}{I} \sqrt{Q^2 + U^2 - \frac{1}{2}(\delta Q^2 + \delta U^2)}, \quad (1)$$

where  $P$  is the debiased polarization fraction and  $I$  is the total intensity.  $Q$ ,  $U$ ,  $\delta Q$ , and  $\delta U$  are the Stokes parameters and their uncertainties. The uncertainty in polarization fraction is estimated using

$$\delta P = \sqrt{\frac{(Q^2 \delta Q^2 + U^2 \delta U^2)}{I^2(Q^2 + U^2)} + \frac{\delta I^2(Q^2 + U^2)}{I^4}}. \quad (2)$$

The polarization position angles were measured increasing toward the east from the north in the sky projection using relation

$$\theta = \frac{1}{2} \tan^{-1}(U/Q). \quad (3)$$

The corresponding uncertainties in  $\theta$  were calculated using

$$\delta \theta = \frac{1}{2} \frac{\sqrt{Q^2 \delta U^2 + U^2 \delta Q^2}}{(Q^2 + U^2)} \times \frac{180^\circ}{\pi}. \quad (4)$$

The plane-of-sky  $B$ -field orientation is inferred by rotating polarization angles by  $90^\circ$  (assuming that the polarization is caused by elongated dust grains aligned perpendicular to the magnetic field). We have used only the data points where the observed uncertainties in position angles are less than  $20^\circ$ . The large-scale  $B$ -fields are examined using Planck  $850 \mu\text{m}$  (353 GHz) dust emission polarization maps (Planck Collaboration et al. 2015, 2016). The image is smoothed to the  $7'$  resolution to ensure good S/N data. The vectors are drawn at  $3'.5$  (half-resolution) steps.

<sup>33</sup> <http://starlink.eao.hawaii.edu/docs/sc22.pdf>

<sup>34</sup> This value was measured using SCUBA2-MAPSTATS recipe under PICARD package in STARLINK.



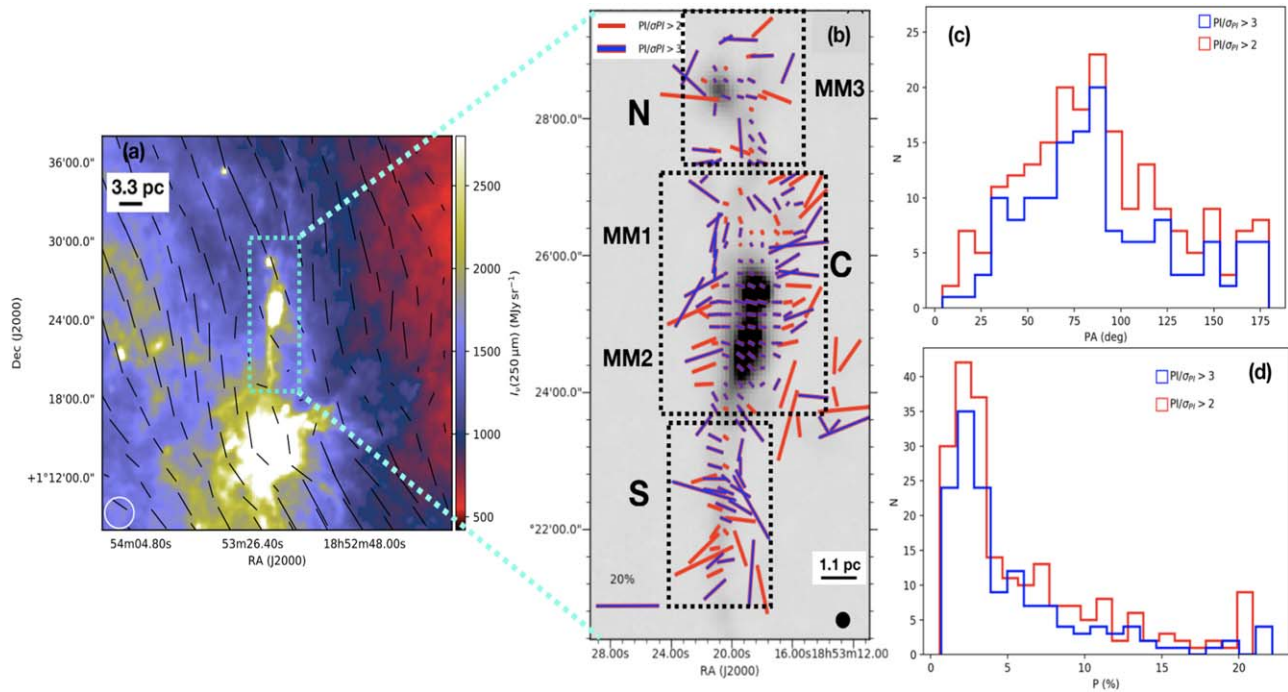


**Figure 2.** Panel (a) shows the large-scale  $B$ -field morphology toward G34 region obtained from Planck 353 GHz dust polarization observations overlaid on the *Herschel* 250  $\mu\text{m}$  image. The location of G34 is inside the cyan dashed rectangle in the center. The Planck beam size is shown as an open circle. Panel (b) shows the smoothed (the 12'' pixel)  $B$ -field orientation in G34 filament from 850  $\mu\text{m}$  POL-2 observations. The background grayscale image shows the dust continuum intensity image. Three regions, “N,” “C,” and “S,” are labeled and the JCMT beam size is shown as a solid circle. The vectors correspond to data with  $PI/\sigma_{PI} > 2$  (red) and  $PI/\sigma_{PI} > 3$  (purple). The scale vector with 20% polarization is also shown. Panels (c) and (d) are distributions of position angle and polarization fraction for the two data sets, respectively.

We checked the quality of our data used for analysis by examining the different S/N values derived from polarization intensity (PI) and its uncertainty ( $\sigma_{PI}$ ). In panel (b) of Figure 2, the  $B$ -fields inferred from  $S/N > 2$  ( $PI/\sigma_{PI} > 2$ ; 211 red vectors) and  $S/N > 3$  ( $PI/\sigma_{PI} > 3$ ; 146 purple vectors) are generally consistent in the regions where both are available. The other two panels (c) and (d) of Figure 2 show comparisons of the distributions of  $B$ -field position angles and polarization fraction of the two subsamples. The aim is to test the validity of the data with  $2 < S/N < 3$  (which is generally used in such studies) and to decide whether or not data with  $S/N \geq 2$  could be used for studying  $B$ -field morphology and strength. The very similar trends in distributions of position angles and polarization percentages reassures us that we can use the  $2 < S/N < 3$  data for further analysis.

### 3. Results and Discussion

The Stokes  $I$  map of the G34 filament in 850  $\mu\text{m}$  continuum emission with inferred  $B$ -field geometry is shown in panel (b) of Figure 2. The elongated shape of the filament is clearly visible and three regions of interest (“N,” “C,” and “S”) are indicated by labeled dashed black rectangles. The overall filament appears to have a small head to the north (containing MM3), a dense clump (consisting of MM1 and MM2) in the center, and a diffuse tail-like structure to the south.

#### 3.1. Magnetic Field Morphology

Panel (a) in Figure 2 represents the large-scale  $B$ -fields inferred from Planck measurements in the region containing G34 (Planck Collaboration et al. 2015). There is a clear indication of field lines aligned in the southwest to northeast

directions. Panel (b) of the figure shows zoomed-in  $B$ -fields in G34 from our POL-2 observations at subparsec scales. The lengths of the line segment are proportional to the fractional polarization. Magnetic field geometry and properties are studied individually in the regions center (C), north (N), and south (S) labeled in panel (b). The northern part containing MM3, has field orientations almost along the elongated clump. The central region, however, has field lines perpendicular to the long axis of the filament with an apparent smooth change in orientation when seen from west to east. The southern diffuse region has most field lines closely perpendicular to the tail. The large-scale field in the northern region from Planck observations is also nearly parallel to the filament (see left panel (a)), which is similar to the fields seen in the region “N” from POL-2 observations. This suggests that the  $B$ -field is connected from parsec to subparsec scales, despite orders of magnitude difference in density and the physical scales. However, it should also be noted that compared to G34, the region measured by Planck next to it is mostly background and foreground. Hence, it is not evident a priori that the field orientations are identical. We found that the background subtraction would tend to make Planck polarization vectors more perpendicular to the filament but details depend on the selection of the reference regions chosen to represent the background and the filament remains unresolved in the Planck data.

Figure 3 shows a better view of magnetic field morphology in the G34 filament where we use the normalized vectors with their lengths independent of the polarization fraction. The smooth change in field lines from being perpendicular to almost parallel from the center to north regions can be clearly seen in this figure.

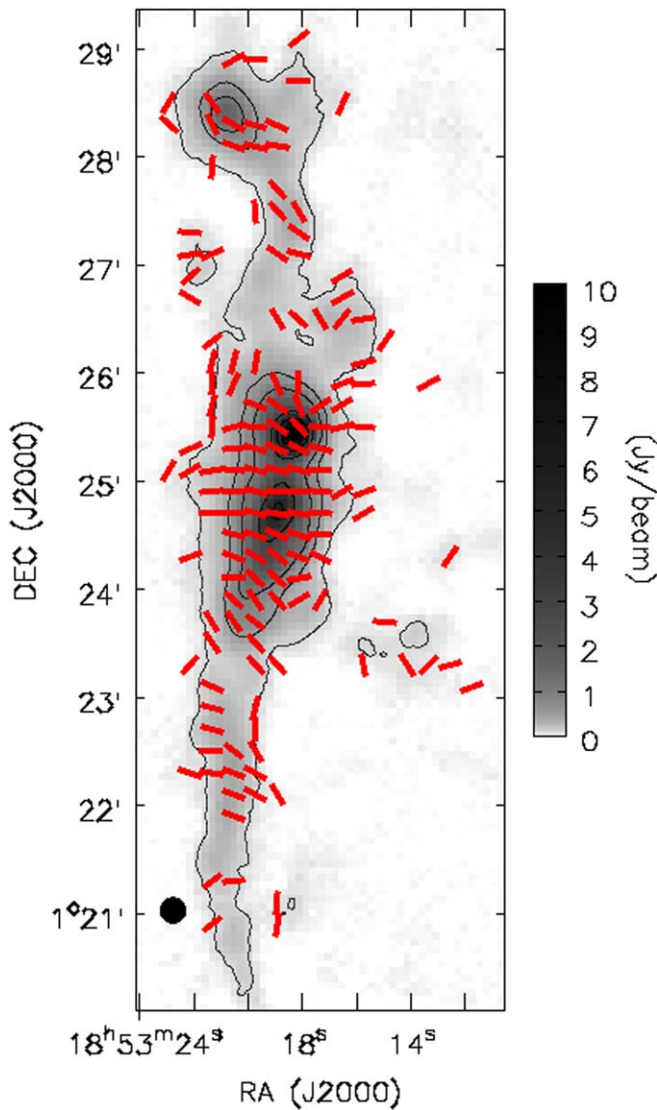


**Figure 3.**  $B$ -field orientation (after  $90^\circ$  rotation of the polarization vectors) in G34 shown with normalized line segments independent of polarization fraction and correspond to  $PI/\sigma_{PI} > 3$  and  $I/\delta I > 10$ , where  $I$  and  $\delta I$  are the total intensity and its uncertainty, respectively. The background image shows the  $850 \mu\text{m}$  continuum emission overlaid with contours of levels [0.1, 0.5, 1.0, 3.0, 5.0, 7.0, 9.0]  $\text{Jy beam}^{-1}$ . JCMT beam size is shown with a black solid circle.

Figure 4 shows the Gaussian fitted distributions of  $B$ -field position angles in the center, north, and south regions. The distributions in all regions peak around  $75^\circ$ , which is close to an east–west orientation.

### 3.2. Dust Temperature and Column Density

We estimated the dust temperature ( $T_d$ ) and  $\text{H}_2$  column density ( $N_{\text{H}_2}$ ) of the G34 filament using archival *Herschel* PACS/SPIRE (70, 160, 250, 350, and  $500 \mu\text{m}$ ) and JCMT  $850 \mu\text{m}$  data fitted with a modified blackbody function. In this procedure, the different resolution *Herschel* images and JCMT  $850 \mu\text{m}$  image were smoothed to the SPIRE  $500 \mu\text{m}$  FWHM beam size of  $35''$  and reprojected on the same grid. The G34 filament is found embedded in a large-scale molecular cloud in *Herschel* images causing additional emission from surrounding material in the line of sight. In order to obtain an accurate column density for G34, this background was subtracted. Then

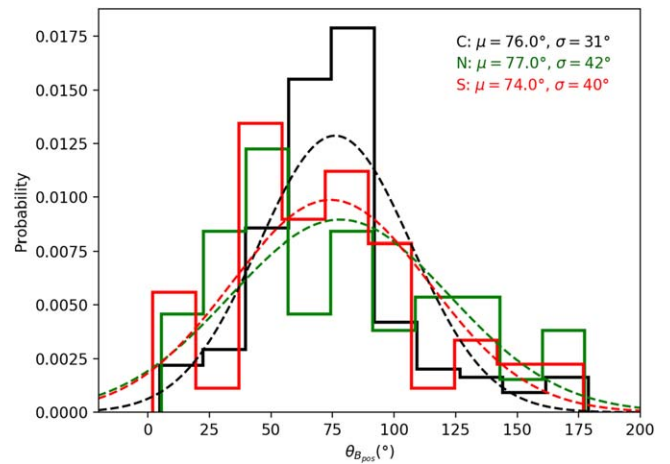


**Figure 4.** Gaussian fitted histograms of the  $B$ -field position angles of data with  $PI/\sigma_{PI} > 2$  in the north (green), south (red), and center (black) of G34.

the spectral energy distribution was fitted to the fluxes obtained in *Herschel* and JCMT maps for each pixel position using the formulae (Kauffmann et al. 2008).

$$I_\nu = B_\nu(T_d)(1 - e^{-\tau_\nu}), \quad (5)$$

$$B_\nu(T_d) = \frac{2h\nu^3}{c^2} \frac{1}{e^{h\nu/k_B T_d} - 1}, \quad (6)$$

$$\tau_\nu = \mu_{\text{H}_2} m_{\text{H}} \kappa_\nu N_{\text{H}_2}, \quad (7)$$

where  $B_\nu(T_d)$  is the Planck function at a given dust temperature ( $T_d$ ),  $\tau_\nu$  is the optical depth,  $\mu_{\text{H}_2}$  is the mean molecular weight per hydrogen molecule,  $m_{\text{H}}$  is the hydrogen atom mass,  $\kappa_\nu$  is the dust opacity (absorption coefficient), and  $N_{\text{H}_2}$  is  $\text{H}_2$  column density. The value of  $\mu_{\text{H}_2}$  is 2.8 and  $\kappa_\nu$  for each used frequency are 1.76, 0.4, 0.195, 0.1, 0.05, and  $0.0197 \text{ cm}^2 \text{ g}^{-1}$ , respectively, adopted from Ossenkopf & Henning (1994) for a dust-to-gas ratio of 0.01. The temperature and column density maps of G34 made using this procedure are shown in Figure 5. The temperatures (left panel of Figure 5) throughout the filament vary from  $\sim 10$  to 25 K with hot dust present in the central region containing MM1/MM2 and colder in the north and southern regions. The column density values (right panel of Figure 5) are found peaking at  $\sim 10^{23} \text{ cm}^{-2}$  in the central region.

We also estimated the  $\text{H}_2$  volume densities of the three regions of G34 north, center, and south assuming them to have cylindrical geometry and adopting the procedure explained in Section 3.2 of Liu et al. (2018a). The projected lengths ( $L$ ) of the cylinders corresponding to ‘‘N,’’ ‘‘C,’’ and ‘‘S’’ regions of G34 shown in the middle panel of Figure 2 are 1.9, 3.0, and 2.6 pc, respectively. The mean values of the projected radius ( $r$ ) of circular ends of these cylinders are measured to be 1.8, 2.2, and 1.1 pc, respectively. We used these values to estimate volumes of the cylinders and their number densities. The estimated values of volume densities are shown in Table 1.

The estimated values of column and volume densities are used in Sections 3.3.1 and 3.3.2 for further calculations.

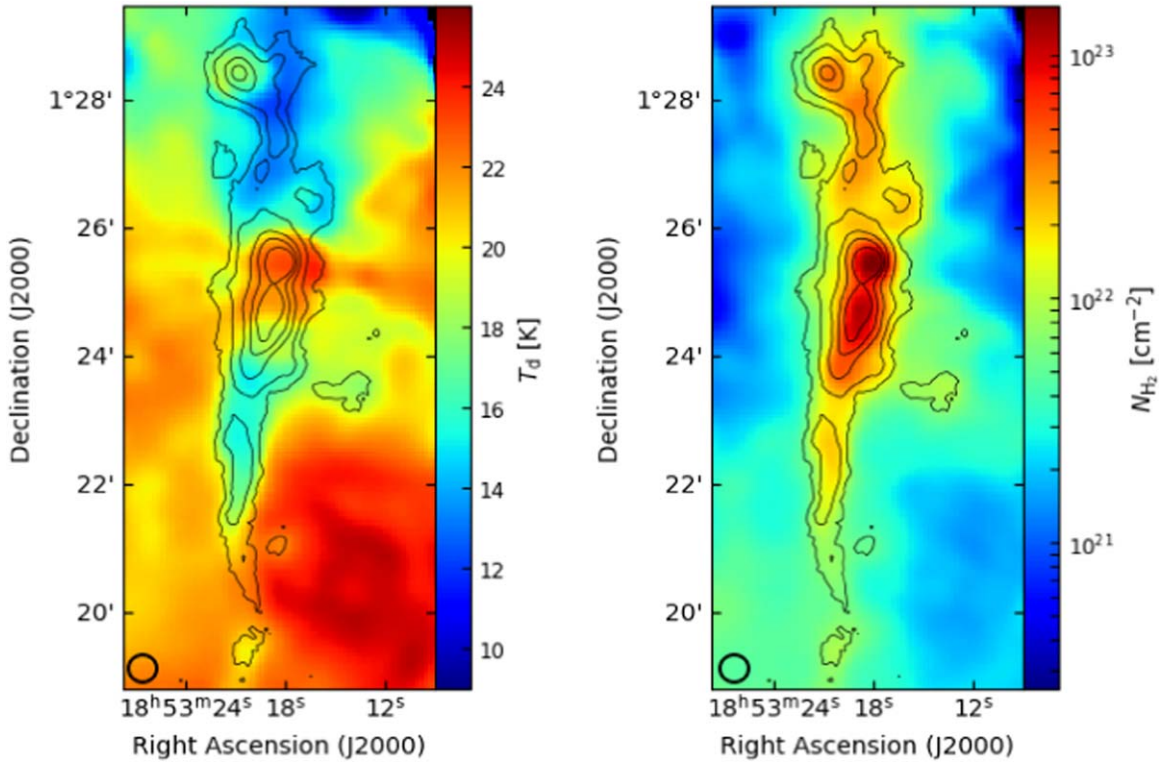


**Figure 5.** Left and right panels show the dust temperature and  $H_2$  column density maps of G34, respectively. The overlaid contours represent  $850 \mu\text{m}$  emission.

**Table 1**  
Values Calculated in G34 Center, North, and South Regions

Region	$\sigma_\theta$ ( $^\circ$ )	$\Delta v$ ( $\text{km s}^{-1}$ )	$n_{H_2}$ ( $\text{cm}^{-3}$ )	$B_{\text{pos}}$ ( $\mu\text{G}$ )	$\lambda_{\text{corr}}$	$M_A$
Center	$11 \pm 4$	$1.1 \pm 0.1$	$1.8 \times 10^5$	$470 \pm 190$	$0.8 \pm 0.4$	$0.34 \pm 0.13$
North	$16 \pm 9$	$0.8 \pm 0.2$	$0.6 \times 10^5$	$100 \pm 40$	$1.1 \pm 0.8$	$0.53 \pm 0.30$
South	$15 \pm 8$	$0.6 \pm 0.2$	$0.2 \times 10^5$	$60 \pm 34$	$0.9 \pm 0.5$	$0.49 \pm 0.26$

### 3.3. Magnetic Field, Gravity, and Turbulence in G34

#### 3.3.1. Magnetic Field Strength

We estimate the plane-of-sky  $B$ -field ( $B_{\text{pos}}$ ) strengths in the central dense region ‘‘C,’’ north ‘‘N,’’ and south ‘‘S’’ regions of G34 using the Davis–Chandrasekhar–Fermi relation (DCF; Davis 1951; Chandrasekhar & Fermi 1953). The DCF relation assumes a regular field geometry with dispersion indicating a measure of the distortion in the field geometry caused by turbulence. The vector distribution is considered to be Gaussian with a well-characterized standard deviation. The DCF method is represented by the expression

$$B_{\text{pos}} = Q \sqrt{4\pi\rho} \frac{\sigma_v}{\sigma_\theta}, \quad (8)$$

where  $\rho$  is the gas density,  $\sigma_v$  is the observed velocity dispersion of the gas, and  $\sigma_\theta$  is the dispersion in polarization angle. The DCF field model assumes that  $Q$  is a factor of order unity that accounts for variations in the  $B$ -field on scales smaller than the beam. Ostriker et al. (2001) compared their mean values of the known plane-of-the-sky magnetic fields with DCF estimates and found  $Q$  in the range of 0.46–0.51. They suggested that the DCF estimate, modified by a multiplicative factor of  $\sim 0.5$  to account for a more complex

magnetic field and density structure, can provide an accurate value of  $B$ -field strength when polarization angles are quite uniform. Therefore, we adopted  $Q$  as 0.5 for our calculations. Following the simplification introduced by Crutcher et al. (2004), Equation (8) can be written as

$$B_{\text{pos}} \approx 9.3 \sqrt{n(H_2)} \frac{\Delta v}{\sigma_\theta} \mu\text{G}, \quad (9)$$

where  $n(H_2)$  is the number density of molecular hydrogen in  $\text{cm}^{-3}$ ,  $\Delta v = \sigma_v \sqrt{8 \ln 2}$  is FWHM in  $\text{km s}^{-1}$  and  $\sigma_\theta$  is in degrees.

The uncertainty in field strength is measured by combining uncertainties using the relation

$$\frac{\delta B_{\text{pos}}}{B_{\text{pos}}} = \frac{1}{2} \frac{\delta n(H_2)}{n(H_2)} + \frac{\delta \Delta v}{\Delta v} + \frac{\delta \sigma_\theta}{\sigma_\theta}, \quad (10)$$

where  $\delta n(H_2)$ ,  $\delta \Delta v$ , and  $\delta \sigma_\theta$  are the uncertainties in  $n(H_2)$ ,  $\Delta v$ , and  $\sigma_\theta$ , respectively.

Tang et al. (2019) has recently investigated the magnetic field strengths in MM1, MM2, and MM3 regions using CSO/SHARP polarization data at  $350 \mu\text{m}$  wavelength and  $N_2H^+(J=1-0)$  line observations. We used their velocity dispersion in  $N_2H^+(J=1-0)$  line with FWHM  $\Delta v = 1.1 \pm 0.1 \text{ km s}^{-1}$ .



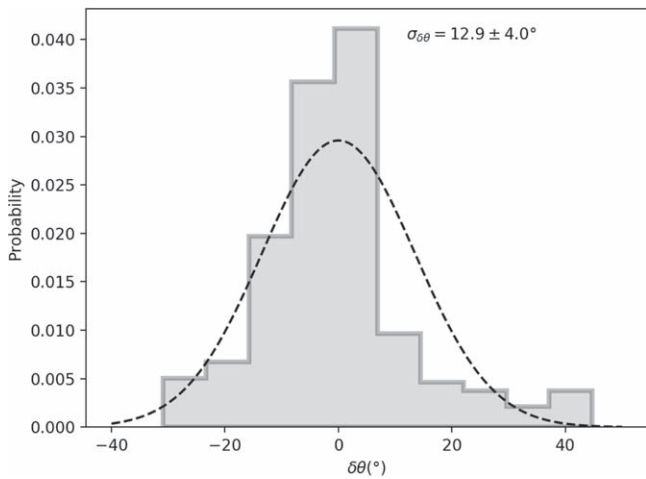


**Figure 6.** Distribution of residual position angles ( $\delta\theta$  with  $\text{PI}/\sigma_{\text{PI}} > 3$ ) in the central region of G34.

We estimated the average volume densities as  $\sim 1.8 \times 10^5 \text{ cm}^{-3}$  in the central region containing MM1/MM2,  $\sim 0.6 \times 10^5 \text{ cm}^{-3}$ , and  $\sim 0.2 \times 10^5 \text{ cm}^{-3}$  in the north and south regions, respectively. We subtracted the mean value of position angles from all measured position angles (with  $\text{PI}/\sigma_{\text{PI}} > 3$ ) in region “C” giving residual angles ( $\delta\theta$ ). The Gaussian fit to the distribution of  $\delta\theta$  values provides a dispersion in position angle ( $\sigma_\theta$ ) of  $12.9 \pm 4.0^\circ$  (see Figure 6). We corrected the value of  $\sigma_\theta$  by a mean value of observed position angle uncertainties, which is measured to be  $7.0^\circ$ . The corrected value of  $\sigma_\theta$  is  $\sqrt{12.9^2 - 7.0^2} \approx 10.8^\circ$ . This value of dispersion in position angles satisfies one of the assumptions of the DCF relation, which limits the maximum value of  $\sigma_\theta$  to be  $\leq 25^\circ$  (Heitsch et al. 2001). Using the abovementioned values of FWHM in  $\text{N}_2\text{H}^+(J=1-0)$ ,  $n(\text{H}_2)$ , and  $\sigma_\theta$ , the strength of  $B_{\text{pos}}$  in G34 center is found to be  $470 \pm 190 \mu\text{G}$ . This field strength is similar to that found in other IRDCs such as  $\sim 270 \mu\text{G}$  in G11.11–0.12 (Pillai et al. 2015) and  $\sim 100 \mu\text{G}$  in G035.39–00.33 (Liu et al. 2018a) but smaller than the value  $790 \mu\text{G}$  in G9.62+0.19 (Liu et al. 2018b).

We have used a similar approach as that described above to estimate the magnetic field strengths in the north and the south regions of G34. The values of velocity dispersion i.e., FWHM of  $\text{N}_2\text{H}^+(J=1-0)$  in these regions are adopted from Tang et al. (2019) for estimating the field strength using Equation (9). Dispersion in position angles toward these regions is estimated similarly as described above for the central region. The uncertainties in  $B_{\text{pos}}$  are estimated using Equation (10), which is derived from Equation (9) by propagating the errors in the quantities. We found the values of  $B_{\text{pos}}$  as  $100 \pm 40 \mu\text{G}$  and  $60 \pm 34 \mu\text{G}$  in “N,” and “S” regions, respectively.

### 3.3.2. Mass-to-flux Ratio

We will use our estimates of magnetic field strength to calculate the standard parameters of mass-to-flux ratio ( $M/\phi_B$ ) and Alfvénic Mach number ( $M_A$ ). These measure the relative importance of magnetic fields versus gravity and turbulence, respectively.

$M/\phi_B$  is the ratio of the mass ( $M$ ) of the object to the flux ( $\phi_B$ ) of the magnetic fields threading the object. Crutcher et al. (2004; and references therein) discussed that the maximum mass that can be supported by a given magnetic flux is known as *critical mass*,  $M_{\text{crit}} = \frac{\phi_B}{2\pi\sqrt{G}}$ . We tested the importance of

the  $B$ -field in the context of gravity in all three regions of G34 where plane-of-sky  $B$ -field strength is estimated using Equation (9). This can be investigated by calculating the value of the criticality parameter ( $\lambda_{\text{obs}}$ ) using the relation

$$\lambda_{\text{obs}} = \frac{(M/\phi)_{\text{obs}}}{(M/\phi)_{\text{crit}}}, \quad (11)$$

where the observed mass-to-flux ratio is estimated as

$$(M/\phi)_{\text{obs}} = \frac{\mu m_{\text{H}} N_{\text{H}_2}}{B_{\text{pos}}}, \quad (12)$$

and  $\mu$ ,  $m_{\text{H}}$ , and  $N_{\text{H}_2}$  are the mean molecular weight per  $\text{H}_2$  molecule, mass of atomic hydrogen, and molecular hydrogen column density, respectively. The average values of column densities in the center, north, and south regions are found to be  $\sim 15 \times 10^{22}$ ,  $4.5 \times 10^{22}$ , and  $2.5 \times 10^{22} \text{ cm}^{-2}$ , respectively.

The clouds that are not collapsing due to the support by magnetic fields are called magnetically “subcritical” ( $\lambda < 1$ ), whereas those with gravity that overcomes the support of the magnetic field are referred to as magnetically “supercritical” ( $\lambda > 1$ ).

$$(M/\phi)_{\text{crit}} = \frac{1}{2\pi\sqrt{G}}. \quad (13)$$

Using the column density in  $\text{cm}^{-2}$  and measured  $B$ -field strength in  $\mu\text{G}$ , we estimated the value of  $\lambda_{\text{corr}}$  after applying a geometric correction to  $\lambda_{\text{obs}}$ , following Crutcher (2004). The value of  $\lambda_{\text{obs}}$  can be overestimated by a factor of 3 due to geometrical effects suggesting  $\lambda_{\text{corr}} = \lambda_{\text{obs}}/3$ . The errors in  $\lambda_{\text{obs}}$  come mainly from the uncertainty in  $B$ -field strength. We calculated the  $\lambda_{\text{corr}}$  in all three regions of G34 and the results are given in Table 1. The values of  $\lambda_{\text{corr}}$  obtained for the center, north, and south show that these regions are transcritical. All the values are close to criticality (i.e.,  $\lambda = 1$ ) suggesting that gravity and magnetic fields are equally important in these regions.

### 3.3.3. B-fields and Turbulence

The nature of turbulent motions in the G34 clump can be studied by estimating the value of  $M_A$ , which describes the relative importance of magnetic fields and turbulence in molecular clouds (Padoan et al. 2001; Nakamura & Li 2008). When the fields are uniform and strong, the turbulence is regulated by the magnetic fields, yielding a sub-Alfvénic scenario (with  $M_A \leq 1$ ). On the other hand, if the cloud is super-Alfvénic (i.e.,  $M_A > 1$ ), the magnetic field is not strong enough to resist scrambling by turbulent motions. The value of  $M_A$ , using molecular line and polarization observations, can be estimated as

$$M_A = \frac{\sqrt{3}\sigma_v}{\sigma_A}, \quad (14)$$

where  $\sigma_v$  is the mean nonthermal velocity dispersion, measured from the FWHM (i.e.,  $\sigma_v = \text{FWHM}/\sqrt{8 \ln 2}$ ) of  $\text{N}_2\text{H}^+(J=1-0)$  line observations Tang et al. (2019), which we used in estimating magnetic field strength.  $\sigma_A$  is the

Alfvénic velocity calculated as

$$\sigma_A = \frac{B_{\text{tot}}}{\sqrt{4\pi\rho}}, \quad (15)$$

Crutcher et al. (2004) found from a statistical study that the total magnetic field strength ( $B_{\text{tot}}$ ) is 1.3 times the plane-of-sky field strength. In the absence of knowledge of the 3D geometry of G34, this is a reasonable correction to apply. The value of  $\sigma_A$  in three regions of G34 is calculated using different magnetic field strengths and volume densities in these regions. Using the values of  $\sigma_v$  and  $\sigma_A$ , we calculate  $M_A$  in all three regions of G34.

The value of dispersion in position angle, FWHM of  $\text{N}_2\text{H}^+(J=1-0)$  line, volume density, estimated plane-of-the-sky magnetic field strength ( $B_{\text{pos}}$ ), projection corrected mass-to-flux ratio ( $\lambda_{\text{corr}}$ ), and Alfvénic Mach number ( $M_A$ ) in regions ‘‘C,’’ ‘‘N,’’ and ‘‘S’’ are given in Table 1. The values of  $\lambda_{\text{corr}}$  in all three regions of G34 suggest it to be marginally critical. The values of Alfvénic Mach number suggest the sub-Alfvénic nature of turbulence in the G34 filament.

Some analytical studies investigated the stability and fragmentation of filaments in the context of turbulent motions (Ostriker 1964; Inutsuka & Miyama 1992; Toalá et al. 2012; Heitsch 2013) and  $B$ -fields (Heitsch 2013) and found that  $B$ -fields are important in filament formation. Soler et al. (2013) studied the dependence of  $B$ -fields on the initial magnetization of filament using a combination of synthetic polarization maps and numerical simulations of magnetized clouds and concluded that strong compression is caused by super-Alfvénic turbulence. Whereas, the sub-Alfvénic turbulence allows the gravitationally collapsing material to move along the  $B$ -field lines (Nakamura & Li 2008). In case of G34, turbulence is found to be sub-Alfvénic in all three regions of G34 and the field lines found to be perpendicular to the elongated axes. This is mostly true in the central and southern regions whereas in the northern region the field appears to change from perpendicular to parallel. However, the field orientation seems mostly perpendicular in the lower part of the northern region. Tang et al. (2019) found a similar geometry in the north part of G34 near MM3 (see Figure 1 for the location of MM3) and suggested that  $B$ -fields must be playing different roles here than in the central region. Liu et al. (2018a) noticed field lines becoming parallel from perpendicular in the northern region of an IRDC G35, suggesting that fields in that region are likely to be poloidal. Similar trend in north of G34 around MM3 agrees with the finding of Tang et al. (2019) and can also indicate that magnetic fields in this region may be poloidal.

### 3.3.4. Structure Function (SF) and Auto-correlation Function (ACF) Analysis

We attempted to separate the large-scale and the turbulent scale  $B$ -fields in the cloud. In the SF method of Hildebrand et al. (2009), the magnetic field consists of large-scale structure,  $B_0$  and a turbulent component,  $\delta B$ . The SF analysis provides the variation of angular dispersion of position angles obtained from polarization observations as a function of separation length  $\ell$ . The turbulent component  $\delta B$  reaches the maximum at some scale larger than the turbulent-scale  $\delta$ . At scales smaller than  $d$  (where  $d$  is the correlation length scale that characterizes the variation in  $B_0$  Hildebrand et al. 2009), the higher-order terms in a Taylor expansion of regular component  $B_0$  can be ignored. In case of  $\delta < \ell \ll d$ , the angular dispersion function can be

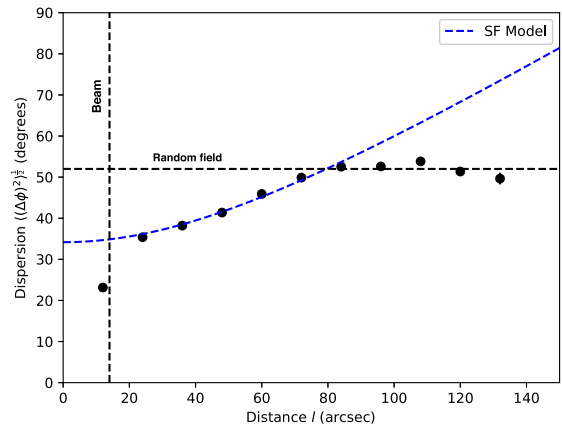


**Figure 7.** Angular dispersion function of G34 central region with angle dispersion segments shown with black solid circles and associated error bars. The best fit is shown with a blue dashed line. The vertical dashed line indicates the JCMT beam size of 14'' and horizontal dashed line shows the value of angular dispersion function expected for a random field (52°, Poidevin et al. 2010).

written as:

$$\langle \Delta\phi^2(l) \rangle_{\text{tot}} \simeq b^2 + m^2 l^2 + \sigma_M^2(l), \quad (16)$$

where  $\langle \Delta\phi^2(l) \rangle_{\text{tot}}$  is the square of the total measured dispersion function, where  $b^2$  is a constant turbulent contribution,  $m^2 l^2$  is the contribution from the large-scale field structure, and  $\sigma_M^2(l)$  is the contribution of the measured uncertainty. The ratio of the turbulent to large-scale magnetic field components given by

$$\frac{\langle \delta B^2 \rangle^{1/2}}{B_0} = \frac{b}{\sqrt{2 - b^2}}, \quad (17)$$

and  $B_0$  is estimated as

$$B_0 \simeq \sqrt{(2 - b^2) 4\pi\mu_{\text{H}} n_{\text{H}_2}} \frac{\sigma_v}{b}. \quad (18)$$

$B_{\text{pos}}$  is corrected by using a correction factor  $Q$  as

$$B_{\text{pos}} = QB_0. \quad (19)$$

The value of  $Q$  is taken as 0.5. The angular dispersion function (ADF) corrected by uncertainty ( $\langle \Delta\phi^2(l) \rangle_{\text{tot}} - \sigma_M^2(l)$ ) is shown in Figure 7 plotted as a function of distance measured in the polarization map. We followed Hildebrand et al. (2009) and divided data into separate distance bins with separations corresponding to the pixel size. At the scales of 0''–25'', the ADF increases steeply, probably due to the contribution from the turbulent field. After 25'' length, the dispersion function increases with shallower slope, which may be a contribution from the large-scale regular magnetic fields. It reaches the maximum at  $\sim 90''$ , the maximum ADF value seen here is less than 52° the one expected for random field structure (Poidevin et al. 2010). The SF is fitted over 25'' <  $l$  < 90''. The calculated parameters are given in Table 2.

The ACF method (Houde et al. 2009) is the expansion of SF analysis with the inclusion of the effects of signal integration along the line of sight and within the beam. The ADF by



**Table 2**  
Parameters Derived from Modified DCF Methods without and with Correction for Beam Integration

Parameters	Description	Without Correction for Beam Integration		With Correction for Beam Integration	
		SF	ACF	SF	ACF
$\Delta\theta$ (")	Angular dispersion	$26.0 \pm 0.3$	$23.2 \pm 2.7$	$52.0 \pm 2.8$	$54.0 \pm 5.1$
$\langle\delta B^2\rangle/\langle B_0^2\rangle$	Turbulent-to-ordered magnetic field energy ratio	$0.21 \pm 0.02$	$0.16 \pm 0.01$	$0.90 \pm 0.04$	$0.81 \pm 0.01$
$B_{\text{pos}}$ ( $\mu\text{G}$ )	Plane-of-sky magnetic field strength	$300 \pm 120$	$200 \pm 70$	$150 \pm 90$	$90 \pm 50$

Houde et al. (2009) is written as

$$1 - \langle \cos[\Delta\phi(l)] \rangle \simeq \frac{1}{N} \frac{\langle \delta B^2 \rangle}{\langle B_0^2 \rangle} \times [1 - e^{-l^2/2(\delta^2+2W^2)}] + a_2'l^2, \quad (20)$$

where  $\Delta\phi(l)$  is the difference between the position angles at a separation of  $l$ ,  $W$  is the beam radius ( $6''$  in case of JCMT which is the FWHM beam divided by  $\sqrt{8 \ln 2}$ ),  $a_2'$  is the slope of second-order term in the Taylor expansion, and  $\delta$  is the turbulent correlation length.  $N$  is the number of turbulent cells in the telescope beam, which is given by

$$N = \frac{(\delta^2 + 2W^2)\Delta'}{\sqrt{2\pi}\delta^3}, \quad (21)$$

where  $\Delta'$  is the effective thickness of the cloud derived from the distance corresponding to the half maximum of polarized flux of the cloud (Houde et al. 2009). The ordered magnetic field strength can be estimated using

$$B_0 \simeq \sqrt{4\pi\mu m_{\text{H}} n_{\text{H}_2} \sigma_v} \left[ \frac{\langle \delta B^2 \rangle}{\langle B_0^2 \rangle} \right]^{-1/2}. \quad (22)$$

The upper panel in Figure 8 shows the ADF of polarization segments in the G34 ‘‘C’’ region. The lower panel of the figure shows the correlated component of the dispersion function. The function is fitted at  $l < 90''$  distance. The reduced  $\chi^2$  of the fitting is 5.3. The turbulent correlation length  $\delta$  is  $7''.4 \pm 0''.9$  ( $0.13 \pm 0.02$  pc). As mentioned above, the turbulent correlation length characterizes the turbulent component of magnetic fields. This is typically the size of a turbulent magnetized cell. Some previous studies have reported values of the turbulent correlation lengths as  $\sim 16$  mpc and  $\sim 10$  mpc in the high-mass star-forming regions OMC1 (Houde et al. 2009) and Orion KL (Houde et al. 2011). In the starless core Oph-C, Liu et al. (2019) reported a correlation length of  $\sim 4.3$  mpc. All these regions are much closer compared to G34. The turbulent correlation length in G34 is larger compared to nearby regions due to insufficient power to resolve it at 3.7 kpc. The number of turbulent cells in G34 is derived as  $5.5 \pm 0.3$ . Other calculated parameters are given in Table 2. The uncertainties in derived parameters are statistical uncertainties from the dispersion function method. The uncertainty in  $B_{\text{pos}}$  is taken as a factor of two, as seen in other measurements in several studies. We did not perform this analysis on the northern and southern regions as we do not have enough vectors (20–25 vectors only) for dispersion function analysis and the ADF is too scattered to fit the function. A detailed investigation of change in estimated parameters of SF and ACF analysis on correction with and without beam integration methods can be found in Liu et al. (2019).

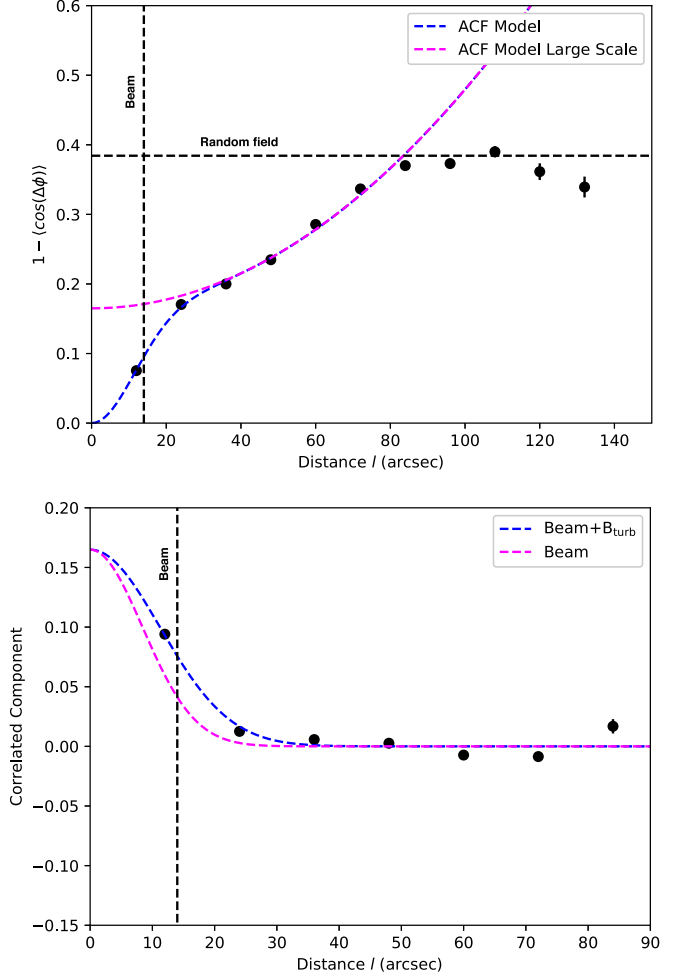


**Figure 8.** Upper panel: angular dispersion function for the G34 central region with angle dispersion segments shown by black solid circles. The bin size is the same as that of Figure 7. The blue dashed curve shows the fitted dispersion function. The pink dashed line shows the large-scale component  $(1/N)\langle\langle\delta B^2\rangle/\langle B_0^2\rangle\rangle + a_2'l^2$  of the best fit. Lower panel: correlated component of the dispersion function  $(1/N)\langle\langle\delta B^2\rangle/\langle B_0^2\rangle\rangle e^{-l^2/2(\delta^2+2W^2)}$  shown by the blue dashed line. The pink dashed line shows the correlated component only due to the beam.

A detailed comparison of magnetic fields, gravity, and turbulence on a filament to core scale in G34 has been presented by Tang et al. (2019) at  $350 \mu\text{m}$ . In this work, we are comparing these quantities in three different regions of the filament using our POL-2 measurements at  $850 \mu\text{m}$ .

### 3.4. Comparison to Other Studies

There have been several attempts to investigate the  $B$ -fields in the G34 filament in various wavelengths using dust and line emission polarization measurements. Figure 9 shows the field

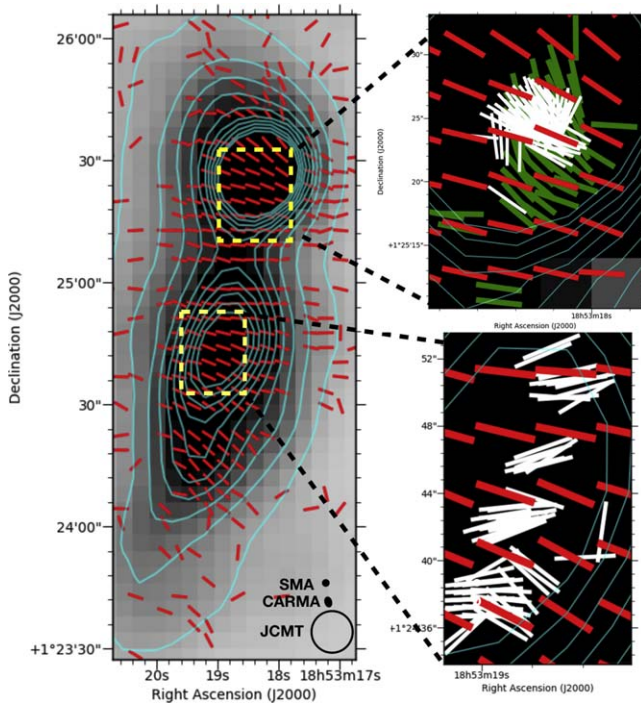


**Figure 9.** Left panel shows  $I_{850\ \mu\text{m}}$  (gray map with cyan contours) and the  $B$ -field vectors (red lines) in the central clump of G34 obtained from POL-2. The data plotted here correspond to  $PI/\sigma_{PI} > 2$ . The regions of CARMA and SMA observations are marked with the yellow dashed rectangles. Right panel shows the zoomed-in regions with the  $B$ -field mapped from CARMA 1.3 mm observations in the MM1 core (green lines) and from SMA observations at  $870\ \mu\text{m}$  (white lines). The resolutions of POL-2, CARMA and SMA observations are  $14''$ ,  $2''.5$ , and  $1''.5$ , respectively. The labeled beam-sizes are shown in the left panel.

morphologies mapped by JCMT/POL-2 (this work), TADPOL/CARMA<sup>35</sup> (Hull et al. 2014), and the SMA<sup>36</sup> (Zhang et al. 2014) observations toward the G34 center containing MM1 and MM2. The field orientation seems to be similar from large to small scales when seen from POL-2 (red vectors) and TADPOL observations (green vectors). But the field geometry changes on even smaller scales seen with the SMA (white vectors). The difference in the POL-2 and SMA field geometries can be seen in the zoomed-in lower right panel of Figure 9 where white line segments are misaligned with red lines. A quantitative comparison using histograms of  $B$ -field position angles from JCMT, CSO, SMA, and CARMA is shown in Figure 10. The details of these other investigations of  $B$ -fields in G34 are given below.

Tang et al. (2019) studied the details of magnetic fields in the regions of G34 containing MM1, MM2, and MM3 using high-resolution (i.e.,  $10''$ )  $350\ \mu\text{m}$  CSO/SHARP polarization observations and kinematics using  $\text{N}_2\text{H}^+(1-0)$  line observations. The  $B$ -field orientation found perpendicular to the main axis of the filament, as also seen in this work, suggests that field lines are guiding material toward the filament. They found a close alignment between local velocity gradients derived from  $\text{N}_2\text{H}^+(1-0)$  line and local  $B$ -field orientation. Since our  $850\ \mu\text{m}$  polarization measurements are consistent with the  $350\ \mu\text{m}$  polarization results of Tang et al. (2019), we expect a similar correlation of local velocity gradients and  $B$ -field lines

<sup>35</sup> Combined Array for Research in Millimeter-wave Astronomy.

<sup>36</sup> Submillimeter Array.

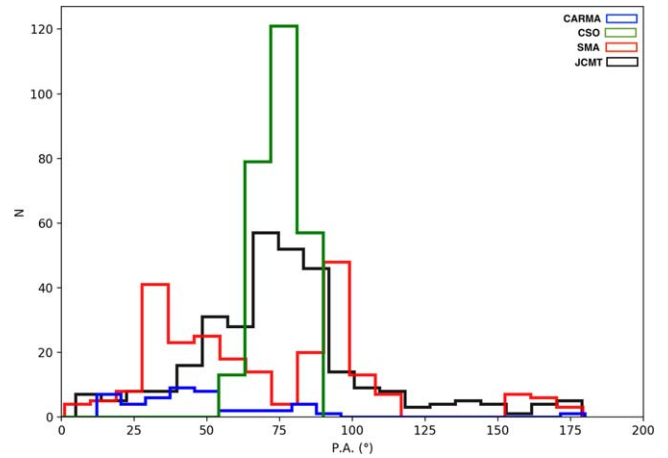


**Figure 10.** Histograms of the  $B$ -field position angles in G34 central region with JCMT, CARMA, CSO, and SMA observations.

at  $850\ \mu\text{m}$ . This kind of correlation suggests a coupling of  $B$ -fields and gas motion in the G34 filament. Tang et al. (2019) also propose varying relative importance of  $B$ -fields, gravity, and turbulence in MM1/MM2 and MM3 resulting in different patterns of small-scale fragmentation in the clumps at a  $0.2\ \text{pc}$  scale. The clump containing MM1 shows no fragmentation at all. They found that clumps containing MM2 show an aligned fragmentation and the other clumps with MM3 show a clustered fragmentation. We refer to Tang et al. (2019) for a detailed explanation of these findings.

Cortes et al. (2008) presented interferometric observations of polarized continuum in 3 mm wavelength (with  $16''$  resolution) and line emission using CO ( $J = 1-0$ ) from the G34 filament using BIMA<sup>37</sup> array. They found a very uniform polarization pattern from both dust and line emission as seen in the present work at  $850\ \mu\text{m}$  and at  $350\ \mu\text{m}$  by Tang et al. (2019). This is a remarkable consistency of polarization measurements in different wavelengths tracing different dust grains.

Hull et al. (2014) studied the  $B$ -fields in G34 central region using  $\lambda = 1.3\ \text{mm}$  TADPOL/CARMA observations of dust polarization with  $2''.5$  resolution. The observations from the present work at  $850\ \mu\text{m}$ , from the CSO at  $350\ \mu\text{m}$  and BIMA at 3 mm wavelength show uniform and ordered field geometry in G34 central region but the results of Hull et al. (2014) reveal a much more complex polarization pattern with a dragged  $B$ -field geometry. They even see a hint of an hourglass morphology in the densest part of the core.

Zhang et al. (2014) investigated the small-scale ( $\leq 0.1\ \text{pc}$ )  $B$ -field structure in G34 center high-density region using SMA at  $870\ \mu\text{m}$  wavelength with  $1''.5$  resolution. Their findings also suggest that the magnetic fields are roughly perpendicular to the major axis of the filament and consistent with those of Hull et al. (2014) in MM1. The SMA polarization measurements are uniform but deviate from our  $850\ \mu\text{m}$   $B$ -field orientations.

The zoomed-in panels of Figure 9 show a deviation in field lines. The subparsec scale fields are misaligned and even become perpendicular to the large-scale field lines. Similarly in the MM2 region, subparsec field lines probed with SMA observations are almost, if not exactly, perpendicular to the large-scale fields seen with JCMT. The field might be strong enough on the clump scale to guide the material along the field

<sup>37</sup> Berkeley-Illinois-Maryland Association.

lines, which eventually get concentrated into cores. The concentration can pinch the  $B$ -field lines inside the cores, but does not necessarily lead to complete misalignment with the large-scale field lines. This may be a potential explanation of the change in field geometry from large clump to small core scales. The MHD simulations by Li & Klein (2019) also revealed the deviation of core scale magnetic fields from large-scale average field orientations with a deviation as strong as  $90^\circ$ . They suggested that change may be caused by the gravitational collapse, enhanced turbulence, and the gas flow along the cloud's long axis.

This can also be explained with numerical simulations (Ostriker et al. 2001; Nakamura & Li 2008; Van Loo et al. 2014) showing less disturbed and organized field geometry when  $B$ -fields are stronger, i.e.,  $\beta = (P_{\text{th}}/P_B) \ll 1$ , where  $\beta$  is the ratio of thermal pressure ( $P_{\text{th}}$ ) to magnetic pressure ( $P_B$ ). To estimate the  $\beta$  values from our observations in G34, we calculated the magnetic pressure ( $P_B = B^2/8\pi$ ) and thermal pressure ( $P_{\text{th}} = nkT$ ), where  $B$  is plane-of-the-sky  $B$ -field strength,  $n$  is the volume density, and  $T$  is the gas temperature (Dirienzo et al. 2015). The values of  $\beta$  are found to be 0.1, 0.2, and 0.6 in the north, central, and southern regions, respectively. Wareing et al. (2016) investigated 3D MHD simulations to understand the formation of clumps and filaments and to determine the driving processes responsible for filament formation and fragmentation. They explored the range of magnetic field strengths in clouds with  $\beta$  varying from 0.1 to 1.0. They found that with no magnetic fields, clumps are found to be forming within the cloud whereas in the case of strong magnetic fields ( $\beta = 0.1$ ) these clumps start appearing as filaments. Our findings of  $\beta$  values in G34 are consistent to these simulations and suggest that  $B$ -fields are playing an important role in the formation of this filament.

Outflow patterns in MM1, MM2, and MM3 of G34 are plotted with SMA polarization measurements in Figure 1 of Zhang et al. (2014). The outflows in MM1 are compact and mostly aligned with the small-scale  $B$ -fields (as seen in their figure) but the outflows in MM2 are highly complex with red- and blueshifted lobes overlapping each other. Therefore, it is hard to check for any correlation in  $B$ -fields and outflows in the core MM2. Sanhueza et al. (2010) reported the discovery of outflows in MM3 using CO ( $J = 3-2$ ) line observations. The outflow mass and kinetic energy associated to outflows in MM3 suggest a high-intermediate mass star embedded in the core. The outflow orientation is not indicated in their work so it is not possible to relate the field orientations and outflow direction in MM3. The authors also report a possible association of outflows with the core MM4 in G34 central region. The highly ordered and the uniform field geometry of G34 seen in the abovementioned studies including the present work, suggests that feedback from these detected outflows associated with MM1, MM2, MM3, and MM4 are not significantly affecting the field geometry of the region. This may be further investigated on much smaller scales using ALMA polarization capabilities.

Among the cores embedded in G34, MM2 has an associated UCH II region (Shepherd et al. 2004). We did not see any prominent change in the  $B$ -field lines due to the compression by the HII region in this core MM2 as seen by Liu et al. (2018b) in an actively high-mass star-forming region G9.62+0.19. The  $B$ -field strength in G34 is found to be less strong than in G9.62

+0.19. To further investigate the effect of UCH II regions on  $B$ -fields in G34-MM2, we have to probe the fields and kinematics at much smaller scales using ALMA observations as done by Dall'Olivo et al. (2019) in G9.62+0.19.

#### 4. Conclusion

We present the plane-of-sky projected magnetic field in G34, obtained using  $850 \mu\text{m}$  dust polarization observations. We investigated the relative importance of gravity, turbulence, and magnetic fields in G34 at subparsec scales. The main findings of the study are as follows:

1. The overall  $B$ -field structure in G34 is ordered and perpendicular to the long axis of the filament. The small-scale field geometry is found connected to the large-scale field lines seen with Planck dust polarization observations. The observed aligned  $B$ -fields in G34 are consistent with theoretical models suggesting that  $B$ -fields play an important role in guiding the contraction of the cloud driven by gravity.
2. Our measurements of field geometry in G34 using JCMT  $850 \mu\text{m}$  wavelength are found consistent with previous studies, which inferred field morphology at  $350 \mu\text{m}$  (CSO) and 3 mm (BIMA) wavelengths. However, there is some deviation in the field lines seen at core scale at  $870 \mu\text{m}$  (SMA) and 1.3 mm (CARMA) wavelengths.
3. The present study, combined with several similar studies of other IRDCs, suggests that field lines are mostly perpendicular to the filament major axes but change direction at subparsec scales in embedded cores, which may be caused by relatively different roles of gravity and  $B$ -fields than that on clump scale.
4. We used an updated form of the Davis–Chandrasekhar–Fermi relation to estimate a plane-of-sky magnetic field strength of  $470 \pm 190 \mu\text{G}$ ,  $100 \pm 40 \mu\text{G}$ , and  $60 \pm 30 \mu\text{G}$  in the central, northern, and southern regions of G34, respectively. Our results are consistent with those found in several other observations of IRDCs and behavior predicted by theoretical simulations.
5. From the estimation of mass-to-flux ratio, the G34 filament is found to be marginally critical with a criticality parameter  $\lambda_{\text{corr}}$  of  $0.8 \pm 0.4$ ,  $1.1 \pm 0.8$ , and  $0.9 \pm 0.5$  in the central, northern, and the southern regions, respectively.
6. The values of Alfvénic Mach number in all three regions correspond to a sub-Alfvénic nature of turbulence in the G34 filament.

The authors thank the referee for a constructive report that considerably helped to improve the content of the manuscript. A. S. and B.-G.A. are supported by National Science Foundation Grant-1715876. T.L. is supported by KASI and EACOA fellowships. A.S. acknowledges the support from Korea Astronomy & Space Science Institute (KASI) for our JCMT observations. M.J., E.R.M., and V.M.P. are supported by Academy of Finland Grant-285769. V.M.P. is also supported by the European Research Council, Advanced grant No. 320773, and the Spanish MINECO under projects MDM-2014-0369 and AYA2017-88754-P. C.W.L. was supported by National Research Foundation of Korea (NRF-2019R1A2C1010851). A.S. thanks Simon Coudé for a useful discussion during the revision and Piyush Bhardwaj



for a critical reading of the draft. This work was carried out in part at the Jet Propulsion Laboratory, operated for NASA by CalTech. D.J. is supported by National Research Council Canada and an NSERC Discovery Grant. W.K. was supported by Basic Science Research Program through the National Research Foundation of Korea (NRF-2016R1C1B2013642). JCMT is operated by the East Asian Observatory on behalf of the National Astronomical Observatory of Japan; Academia Sinica Institute of Astronomy and Astrophysics; the Korea Astronomy and Space Science Institute; the Operation, Maintenance and Upgrading Fund for Astronomical Telescopes and Facility Instruments, budgeted from the Ministry of Finance of China and administrated by the Chinese Academy of Sciences and, the National Key R&D Program of China (No. 2017YFA0402700). J.L. and K.Q. are supported by National Key R&D Program of China No. 2017YFA0402600, and acknowledge the supports from National Natural Science Foundation of China (grant Nos. U1731237, 11473011, 11590781, and 11629302). K.W. acknowledges support by the National Key Research and Development Program of China (2017YFA0402702), the National Science Foundation of China (11973013, 11721303), and the starting grant at the Kavli Institute for Astronomy and Astrophysics, Peking University (7101502016).

*Facility:* James Clerk Maxwell telescope (JCMT).

*Softwares:* Starlink (Currie et al. 2014), Astropy (Astropy Collaboration et al. 2013).

### ORCID iDs

Archana Soam  <https://orcid.org/0000-0002-6386-2906>  
 Tie Liu  <https://orcid.org/0000-0002-5286-2564>  
 B-G Andersson  <https://orcid.org/0000-0001-6717-0686>  
 Chang Won Lee  <https://orcid.org/0000-0002-3179-6334>  
 Junhao Liu  <https://orcid.org/0000-0002-4774-2998>  
 Mika Juvela  <https://orcid.org/0000-0002-5809-4834>  
 Pak Shing Li  <https://orcid.org/0000-0001-8077-7095>  
 Paul F. Goldsmith  <https://orcid.org/0000-0002-6622-8396>  
 Qizhou Zhang  <https://orcid.org/0000-0003-2384-6589>  
 Patrick M. Koch  <https://orcid.org/0000-0003-2777-5861>  
 Kee-Tae Kim  <https://orcid.org/0000-0003-2412-7092>  
 Keping Qiu  <https://orcid.org/0000-0002-5093-5088>  
 Doug Johnstone  <https://orcid.org/0000-0002-6773-459X>  
 Derek Ward-Thompson  <https://orcid.org/0000-0003-1140-2761>  
 James Di Francesco  <https://orcid.org/0000-0002-9289-2450>  
 Ya-Wen Tang  <https://orcid.org/0000-0002-0675-276X>  
 Gwanjeong Kim  <https://orcid.org/0000-0003-2011-8172>  
 Steve Mairs  <https://orcid.org/0000-0002-6956-0730>  
 Patricia Sanhueza  <https://orcid.org/0000-0002-7125-7685>  
 Michael S. Gordon  <https://orcid.org/0000-0002-1913-2682>  
 Ken'ichi Tatematsu  <https://orcid.org/0000-0002-8149-8546>  
 Sheng-Yuan Liu  <https://orcid.org/0000-0003-4603-7119>  
 Kate Pattle  <https://orcid.org/0000-0002-8557-3582>  
 Peregrine M. McGehee  <https://orcid.org/0000-0003-0948-6716>  
 Ke Wang  <https://orcid.org/0000-0002-7237-3856>  
 Sarah F. Graves  <https://orcid.org/0000-0001-9361-5781>  
 Kevin M. Lacaille  <https://orcid.org/0000-0001-9870-5663>  
 Geumsook Park  <https://orcid.org/0000-0001-8467-3736>  
 Woojin Kwon  <https://orcid.org/0000-0003-4022-4132>  
 Eun Jung Chung  <https://orcid.org/0000-0003-0014-1527>  
 Gary Fuller  <https://orcid.org/0000-0001-8509-1818>

### References

- André, P., Di Francesco, J., Ward-Thompson, D., et al. 2014, in *Protostars and Planets VI*, ed. H. Beuther et al. (Tucson, AZ: Univ. Arizona Press), 27
- Astropy Collaboration, Robitaille, T. P., Tollerud, E. J., et al. 2013, *A&A*, 558, A33
- Chambers, E. T., Jackson, J. M., Rathborne, J. M., & Simon, R. 2009, *ApJS*, 181, 360
- Chandrasekhar, S., & Fermi, E. 1953, *ApJ*, 118, 113
- Chapin, E. L., Berry, D. S., Gibb, A. G., et al. 2013, *MNRAS*, 430, 2545
- Chapman, N. L., Goldsmith, P. F., Pineda, J. L., et al. 2011, *ApJ*, 741, 21
- Chen, H.-R., Liu, S.-Y., Su, Y.-N., & Wang, M.-Y. 2011, *ApJ*, 743, 196
- Cortes, P. C., Crutcher, R. M., Shepherd, D. S., & Bronfman, L. 2008, *ApJ*, 676, 464
- Cox, N. L. J., Arzoumanian, D., André, P., et al. 2016, *A&A*, 590, A110
- Crutcher, R. M. 2004, *Ap&SS*, 292, 225
- Crutcher, R. M., Nutter, D. J., Ward-Thompson, D., & Kirk, J. M. 2004, *ApJ*, 600, 279
- Currie, M. J., Berry, D. S., Jenness, T., et al. 2014, in *ASP Conf. Ser. 485, Astronomical Data Analysis Software and Systems XXIII*, ed. N. Manset & P. Forshay (San Francisco, CA: ASP), 391
- Dall'Olio, D., Vlemmings, W. H. T., Persson, M. V., et al. 2019, *A&A*, 626, A36
- Davis, L. 1951, *PhRv*, 81, 890
- Dempsey, J. T., Friberg, P., Jenness, T., et al. 2013, *MNRAS*, 430, 2534
- Dirienzo, W. J., Brogan, C., Indebetouw, R., et al. 2015, *AJ*, 150, 159
- Dolginov, A. Z., & Mitrofanov, I. G. 1976, *Ap&SS*, 43, 291
- Eden, D. J., Liu, T., Kim, K.-T., et al. 2019, *MNRAS*, 485, 2895
- Federrath, C., Rathborne, J. M., Longmore, S. N., et al. 2016, *ApJ*, 832, 143
- Foster, J. B., Arce, H. G., Kassis, M., et al. 2014, *ApJ*, 791, 108
- Friberg, P., Bastien, P., Berry, D., et al. 2016, *Proc. SPIE*, 9914, 991403
- Gómez, G. C., Vázquez-Semadeni, E., & Zamora-Avilés, M. 2018, *MNRAS*, 480, 2939
- Hacar, A., Alves, J., Burkert, A., & Goldsmith, P. 2016, *A&A*, 591, A104
- Hacar, A., Tafalla, M., Kauffmann, J., & Kovács, A. 2013, *A&A*, 554, A55
- Heitsch, F. 2013, *ApJ*, 769, 115
- Heitsch, F., Zweibel, E. G., Mac Low, M.-M., Li, P., & Norman, M. L. 2001, *ApJ*, 561, 800
- Hildebrand, R. H., Kirby, L., Dotson, J. L., Houde, M., & Vaillancourt, J. E. 2009, *ApJ*, 696, 567
- Holland, W. S., Bintley, D., Chapin, E. L., et al. 2013, *MNRAS*, 430, 2513
- Houde, M., Rao, R., Vaillancourt, J. E., & Hildebrand, R. H. 2011, *ApJ*, 733, 109
- Houde, M., Vaillancourt, J. E., Hildebrand, R. H., Chitsazzadeh, S., & Kirby, L. 2009, *ApJ*, 706, 1504
- Hull, C. L. H., Plambeck, R. L., Kwon, W., et al. 2014, *ApJS*, 213, 13
- Inutsuka, S.-I., & Miyama, S. M. 1992, *ApJ*, 388, 392
- Juvela, M., Guillet, V., Liu, T., et al. 2018, *A&A*, 620, A26
- Kauffmann, J., Bertoldi, F., Bourke, T. L., Evans, N. J. I., & Lee, C. W. 2008, *A&A*, 487, 993
- Klassen, M., Pudritz, R. E., & Kirk, H. 2017, *MNRAS*, 465, 2254
- Koch, P. M., Tang, Y.-W., Ho, P. T. P., et al. 2014, *ApJ*, 797, 99
- Lazarian, A., Goodman, A. A., & Myers, P. C. 1997, *ApJ*, 490, 273
- Li, P. S., & Klein, R. I. 2019, *MNRAS*, 485, 4509
- Li, P. S., Klein, R. I., & McKee, C. F. 2018, *MNRAS*, 473, 4220
- Liu, J., Qiu, K., Berry, D., et al. 2019, *ApJ*, 877, 43
- Liu, T., Kim, K.-T., Juvela, M., et al. 2018c, *ApJS*, 234, 28
- Liu, T., Kim, K.-T., Liu, S.-Y., et al. 2018b, *ApJL*, 869, L5
- Liu, T., Li, P. S., Juvela, M., et al. 2018a, *ApJ*, 859, 151
- Molinari, S., Brand, J., Cesaroni, R., Palla, F., & Palumbo, G. G. C. 1998, *A&A*, 336, 339
- Nakamura, F., & Li, Z.-Y. 2008, *ApJ*, 687, 354
- Nguyen Luong, Q., Motte, F., Henneemann, M., et al. 2011, *A&A*, 535, A76
- Ossenkopf, V., & Henning, T. 1994, *A&A*, 291, 943
- Ostriker, E. C., Stone, J. M., & Gammie, C. F. 2001, *ApJ*, 546, 980
- Ostriker, J. 1964, *ApJ*, 140, 1056
- Padoan, P., Goodman, A., Draine, B. T., et al. 2001, *ApJ*, 559, 1005
- Pillai, T., Kauffmann, J., Tan, J. C., et al. 2015, *ApJ*, 799, 74
- Planck Collaboration, Ade, P. A. R., Aghanim, N., et al. 2015, *A&A*, 576, A104
- Planck Collaboration, Ade, P. A. R., Aghanim, N., et al. 2016, *A&A*, 586, A138
- Poidevin, F., Bastien, P., & Matthews, B. C. 2010, *ApJ*, 716, 893
- Rathborne, J. M., Garay, G., Jackson, J. M., et al. 2011, *ApJ*, 741, 120
- Rathborne, J. M., Jackson, J. M., & Simon, R. 2006, *ApJ*, 641, 389
- Rathborne, J. M., Jackson, J. M., Zhang, Q., & Simon, R. 2008, *ApJ*, 689, 1141

- Sakai, T., Sakai, N., Furuya, K., et al. 2015, [ApJ](#), 803, 70
- Sakai, T., Yanagida, T., Furuya, K., et al. 2018, [ApJ](#), 857, 35
- Sanhueza, P., Garay, G., Bronfman, L., et al. 2010, [ApJ](#), 715, 18
- Sanhueza, P., Jackson, J. M., Foster, J. B., et al. 2012, [ApJ](#), 756, 60
- Shepherd, D. S., Nürnberger, D. E. A., & Bronfman, L. 2004, [ApJ](#), 602, 850
- Shepherd, D. S., Povich, M. S., Whitney, B. A., et al. 2007, [ApJ](#), 669, 464
- Soam, A., Pattle, K., Ward-Thompson, D., et al. 2018, [ApJ](#), 861, 65
- Soler, J. D., Hennebelle, P., Martin, P. G., et al. 2013, [ApJ](#), 774, 128
- Tang, Y.-W., Koch, P. M., Peretto, N., et al. 2019, [ApJ](#), 878, 10
- Toalá, J. A., Vázquez-Semadeni, E., & Gómez, G. C. 2012, [ApJ](#), 744, 190
- Van Loo, S., Keto, E., & Zhang, Q. 2014, [ApJ](#), 789, 37
- Wang, J.-W., Lai, S.-P., Eswaraiah, C., et al. 2019, [ApJ](#), 876, 42
- Wang, K., Testi, L., Burkert, A., et al. 2016, [ApJS](#), 226, 9
- Wardle, J. F. C., & Kronberg, P. P. 1974, [ApJ](#), 194, 249
- Ward-Thompson, D., Pattle, K., Bastien, P., et al. 2017, [ApJ](#), 842, 66
- Wareing, C. J., Pittard, J. M., Falle, S. A. E. G., & Van Loo, S. 2016, [MNRAS](#), 459, 1803
- Xu, J.-L., Li, D., Zhang, C.-P., et al. 2016, [ApJ](#), 819, 117
- Yanagida, T., Sakai, T., Hirota, T., et al. 2014, [ApJL](#), 794, L10
- Zhang, Q., Qiu, K., Girart, J. M., et al. 2014, [ApJ](#), 792, 116